

Digital Quantum Simulation of the Holstein-Primakoff Transformation on Noisy Qubits

Kelvin Yip,¹ Alessandro Monteros,¹ Sahel Ashhab,^{2,3} and Lin Tian^{1,*}

¹*School of Natural Sciences, University of California, Merced, California 95343, USA*

²*Advanced ICT Research Institute, National Institute of Information and Communications Technology (NICT), 4-2-1 Nukui-Kitamachi, Koganei, Tokyo 184-8795, Japan*

³*Research Institute for Science and Technology, Tokyo University of Science, 1-3 Kagurazaka, Shinjuku-ku, Tokyo 162-8601, Japan*

Quantum simulation of many-body systems offers a powerful approach to exploring collective quantum dynamics beyond classical computational reach. Although spin and fermionic models have been extensively simulated on digital quantum computers, the simulation of bosonic systems on programmable quantum processors is often hindered by the intrinsically large Hilbert space of bosonic modes. In this work, we study the digital quantum simulation of bosonic modes using the Holstein-Primakoff (HP) transformation and implement this protocol on a cloud-based superconducting quantum processor. Two representative models are realized on quantum hardware: (i) the driven harmonic oscillator and (ii) the Jaynes-Cummings model. Using data obtained from the quantum simulations, we systematically examine the interplay between algorithmic and hardware-induced errors to identify optimal simulation parameters. The dominant algorithmic errors arise from the finite number of qubits used in the HP mapping and the finite number of Trotter steps in the time evolution, while hardware errors mainly originate from gate infidelity, decoherence, and readout errors. This study advances the digital quantum simulation of many-body systems involving bosonic degrees of freedom on currently available cloud quantum processors and provides a framework that can be extended to more complex spin-boson and multimode cavity models.

I. INTRODUCTION

Digital and analog quantum simulations of many-body systems on programmable or tunable quantum processors provide a versatile route for exploring complex quantum dynamics that are intractable for classical computation [1–4]. In recent years, cloud-based quantum platforms such as IBM Quantum (IBMQ) [5] have enabled rapid advances in the experimental realization of digital quantum simulations [6–12]. Leveraging Qiskit and related open-source toolkits [13], a wide variety of models including spin chains and molecular Hamiltonians have been implemented on cloud quantum processors [14–19]. The accessibility of cloud-based quantum processors enables systematic benchmarking of simulation algorithms, circuit optimization strategies, and error-mitigation techniques on real quantum hardware, which is characterized by finite qubit coherence times, non-negligible gate errors, and readout errors [20–31].

Quantum simulation of bosonic models using digital quantum processors is fundamentally challenging due to the intrinsic structure of their Hilbert space. In contrast to spin and fermionic systems, bosonic modes possess an infinitely large Hilbert space [32]. As a result, it is difficult to implement digital quantum simulations of such large Hilbert spaces on noisy quantum processors, which are limited to finite circuit depth and coherence times. To overcome this challenge, analog and hybrid quantum simulation approaches have been employed

to mimic models involving bosonic modes by exploiting other bosonic systems, such as superconducting resonator modes and the harmonic motion of trapped ions [33–35]. These approaches provide a natural solution for simulating bosonic models and have been applied to a broad range of systems, spanning models in the cavity and circuit quantum electrodynamics (QED) setups, realizations of Bose-Fermi mixture models, and strongly correlated bosonic many-body Hamiltonians [36–42]. Meanwhile, digital quantum simulation has also been employed to emulate bosonic systems with a bounded number of excitations and has been implemented across various physical platforms, including nuclear magnetic resonance (NMR) systems, superconducting qubits, and trapped ions [43–52]. In these digital approaches, the bosonic Hilbert space is assumed to be truncated to a finite (and often small) number of excitations, with the Fock states of the bosonic modes mapped onto multi-qubit states. Another theoretical framework that bridges bosonic modes and qubits is the Holstein-Primakoff (HP) transformation [53, 54], which maps bosonic operators to collective angular-momentum operators of spin ensembles, or vice versa. Through this mapping, a bosonic mode can be simulated by a qubit ensemble, enabling the qubits to reproduce bosonic dynamics and emulate a wide range of boson-related phenomena. In Refs. [55, 56], this approach was employed to simulate a spin-boson model, in which both the bosonic (cavity) mode and the spins are encoded using qubits.

In this work, we investigate the digital quantum simulation of the HP transformation using noisy qubits on a cloud-based superconducting quantum processor (IBMQ). By mapping a bosonic mode onto an ensemble

* ltian@ucmerced.edu

of superconducting qubits, we construct quantum circuits that reproduce the time evolution of the bosonic mode. We simulate two representative models involving bosonic degrees of freedom: the driven harmonic oscillator and the Jaynes-Cummings (JC) model, which capture the essential features of bosonic dynamics and their interaction with spins, such as light-matter coupling. Using these simulations, we systematically examine the effects of algorithmic errors arising from the finite number of qubits used in the HP transformation and the finite number of Trotter steps employed in the time evolution, together with hardware noise sources such as finite gate fidelities and readout errors. By comparing results from noiseless classical simulations performed with Qiskit and from executions on real quantum hardware, we identify optimal parameter regimes that maximize the simulation fidelity. In addition, we employ a synthesized-unitary approach to determine optimized circuit configurations for implementing the JC model. Our results demonstrate that digital quantum simulation based on the HP transformation provides a promising framework for exploring quantum dynamics involving bosonic modes and can be applied to studying novel physical phenomena in a wide range of quantum systems.

The remainder of this paper is organized as follows. In Sec. II, we introduce the HP transformation, which maps a bosonic mode onto a spin ensemble, and describe how bosonic operators are represented by collective qubit operators. In Sec. III, we perform quantum simulations of the driven harmonic oscillator using this mapping, present the corresponding quantum circuits implemented on IBMQ, and analyze the effects of the finite number of qubits used in the HP transformation as well as the impact of readout noise on the simulation. In Sec. IV, we simulate the quantum dynamics of the JC model by employing both the Suzuki-Trotter decomposition [57] and the synthesized unitary approaches [58–61]. The impact of two-qubit gate errors of the quantum hardware on the performance of this simulation is assessed. Finally, Sec. V discusses the trade-off between algorithmic and hardware-induced errors and presents the conclusions of this work.

II. HP TRANSFORMATION

Consider an ensemble of N spins (qubits) represented by the Pauli operators $\sigma_{i\pm}$ and σ_{iz} , where $i \in [1, N]$. The collective spin operators are defined as ($\hbar = 1$)

$$J_z = \frac{1}{2} \sum_{i=1}^N \sigma_{iz}, \quad J_{\pm} = \sum_{i=1}^N \sigma_{i\pm}, \quad (1)$$

which are sums of individual spin operators and satisfy the standard angular-momentum commutation relations $[J_+, J_-] = 2J_z$ and $[J_z, J_{\pm}] = \pm J_{\pm}$. In the HP transformation [53], the collective spin operators are mapped to the operators of a single bosonic mode, or vice versa,

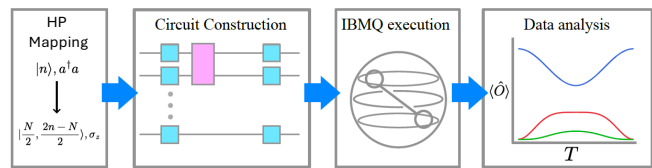


FIG. 1. Schematic workflow of the procedure from mapping a bosonic mode onto a qubit ensemble, circuit construction, IBMQ execution, to the analysis of the measured data. Both classical (noiseless) and quantum simulations are performed

according to

$$J_+ = a^\dagger \sqrt{N - a^\dagger a}, \quad (2a)$$

$$J_- = \sqrt{N - a^\dagger a} a, \quad (2b)$$

$$J_z = a^\dagger a - \frac{N}{2}, \quad (2c)$$

where a (a^\dagger) is the annihilation (creation) operator of the bosonic mode, satisfying the commutation relation $[a, a^\dagger] = 1$. Under this mapping, the bosonic ground state $|0\rangle$ corresponds to the fully polarized spin-down state $|\downarrow\downarrow\cdots\downarrow\rangle = |J, J_z\rangle = |\frac{N}{2}, -\frac{N}{2}\rangle$, where the total spin quantum number is $J = N/2$ and the z -component of the total spin is $J_z = -N/2$. The n th excited oscillator state corresponds to a Dicke state, defined as the fully symmetric superposition of all spin configurations with n spins pointing up and the remaining $N - n$ spins pointing down. These Dicke states form an effective bosonic ladder under the HP mapping, where each excitation corresponds to a single collective spin flip within the ensemble. This correspondence has been widely applied to physical systems such as atomic ensembles, nitrogen-vacancy (NV) center ensembles, and superconducting qubit arrays.

In the large N limit with $N \gg \langle a^\dagger a \rangle$, the square-root factors in Eq. (2) can be approximated by \sqrt{N} , yielding

$$a^\dagger \approx \frac{J_+}{\sqrt{N}}, \quad a \approx \frac{J_-}{\sqrt{N}}. \quad (3)$$

In this regime, the bosonic creation and annihilation operators are effectively represented by normalized collective spin-raising and spin-lowering operators. Using this correspondence, we simulate the time evolution of two representative bosonic systems: the driven quantum harmonic oscillator and the JC model, and implement these simulations on IBMQ. The workflow is illustrated in Fig. 1.

III. DIGITAL SIMULATION OF THE DRIVEN HARMONIC OSCILLATOR

A. Model

A driven quantum harmonic oscillator is described by the Hamiltonian ($\hbar = 1$)

$$H = \omega_0 (a^\dagger a + \frac{1}{2}) + F \cos(\omega_d t) (a + a^\dagger), \quad (4)$$

where ω_0 is the oscillator frequency, ω_d is the driving frequency, and F is the driving amplitude. Assuming $\omega_0, \omega_d \gg |\omega_0 - \omega_d|$, F , the rotating-wave approximation (RWA) can be applied. In the rotating frame defined by $H_0 = \omega_d a^\dagger a$, the Hamiltonian under the RWA becomes

$$H_{\text{rot}} = \Delta a^\dagger a + \frac{F}{2} (a + a^\dagger), \quad (5)$$

where $\Delta = \omega_0 - \omega_d$ is the detuning between the oscillator and the drive, and a constant term $\frac{\omega_0}{2}$ has been omitted. The driving term effectively shifts the origin of the harmonic potential by $d_0 = -F/(\sqrt{2}\Delta)$ along the coordinate axis. Here the coordinate operator of the harmonic oscillator has the form $x = \frac{1}{\sqrt{2}}(a + a^\dagger)$ in terms of the creation and annihilation operators. Starting from the vacuum state $|0\rangle$, the oscillator evolves into a coherent state $|\alpha(t)\rangle$ that oscillates periodically about the displaced origin, with

$$\alpha(t) = \frac{d_0}{\sqrt{2}} [1 - \cos(\Delta t) + i \sin(\Delta t)]. \quad (6)$$

The probability of occupying the n th excited state of the oscillator mode can be derived as:

$$P_b^{(n)} = |\langle n | \alpha(t) \rangle|^2 = e^{-|\alpha|^2} \frac{|\alpha|^{2n}}{n!}, \quad (7)$$

where $|\alpha(t)|^2 = 2d_0^2 \sin^2(\frac{\Delta t}{2})$.

When mapped onto qubit operators using the HP transformation in the large- N limit, Hamiltonian (5) becomes

$$H_{\text{rot}} = \sum_{i=1}^N \left[\frac{\Delta}{2} \sigma_{iz} + \frac{F}{2\sqrt{N}} \sigma_{ix} \right] = \sum_{i=1}^N \Omega \sigma_{i\hat{n}}, \quad (8)$$

where $\Omega = \sqrt{(\frac{\Delta}{2})^2 + (\frac{F}{2\sqrt{N}})^2}$, $\sigma_{i\hat{n}}$ denotes the Pauli operator along the rotated axis \hat{n} , and the constant term $\frac{N\Delta}{2}$ has been neglected. This Hamiltonian contains no qubit-qubit interactions and can therefore be implemented using single-qubit quantum logic gates only. For a single qubit initially prepared in the spin-down state, the time-dependent wavefunction under Eq. (8) is $|\psi_i(t)\rangle = e^{-i\Omega \sigma_{i\hat{n}} t} |\downarrow\rangle_i$. The probability of finding the qubit in the spin-up state is

$$P_\uparrow = \frac{F^2}{4N\Omega^2} \sin^2(\Omega t). \quad (9)$$

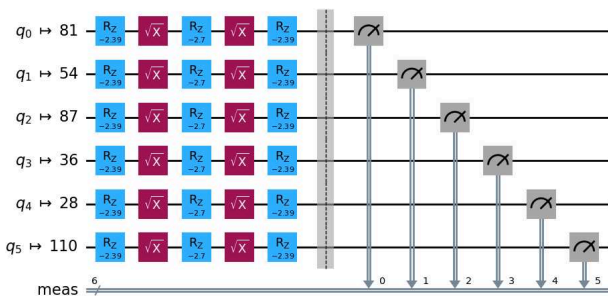


FIG. 2. Circuit diagram for the digital simulation of the driven harmonic oscillator using six qubits, up to a global phase of π . The qubit labels (e.g., 81 and 54) indicate their physical indices on the IBM Torino. The circuit is transpiled into the native IBMQ gate set and followed by qubit measurements. The phases of the R_z gates correspond to the parameters $\Delta = 1$, $F = 0.75$, and evolution time $t = \pi$, and are shown inside the blue boxes of the gates. All parameters are expressed in dimensionless units.

When the Hamiltonian acts on N qubits all initialized in $|\downarrow\rangle$, the probability of measuring n spins in the state $|\downarrow\rangle$, which corresponds to the oscillator Fock state $|n\rangle$, is given by the binomial distribution

$$P_c^{(n)} = \binom{N}{n} P_\uparrow^n (1 - P_\uparrow)^{N-n}. \quad (10)$$

It can be shown that in the limit of $N \gg n$, $P_c^{(n)}$ takes the same form as $P_b^{(n)}(|\alpha|^2)$ in Eq. (7) when $|\alpha|^2 = NP_\uparrow$. In fact, for $|F/\Delta| \ll 1$ (ensuring a small excitation number), we can find that $|\alpha|^2 \approx NP_\uparrow$. Therefore, the excitation statistics of the spin ensemble reproduce the state distribution of the oscillator under the HP mapping.

B. Circuit Implementation and Execution

We perform classical simulations of the driven harmonic oscillator using Qiskit Aer and execute quantum simulations on IBM Torino for a range of qubit numbers. Since the Hamiltonian of the driven harmonic oscillator [Eq. (8)] contains only single-qubit terms, its digital implementation requires only single-qubit quantum logic gates. Figure 2 shows the circuit diagram for a six-qubit realization, where the Hamiltonian evolution is transpiled into the native IBMQ gate set. The qubits in this diagram are labeled as q_i with $i \in [0, 5]$, and their corresponding physical qubit indices on the selected backend are also indicated. In this circuit, the native gates acting on the i th qubit include the z -rotation $R_z(\theta) = e^{-i\frac{\theta}{2}\sigma_{iz}}$ with rotation angle θ , and the SX gate, $\sqrt{X} = e^{-i\frac{\pi}{4}\sigma_{ix}}$. On IBMQ, R_z rotations are implemented virtually through frame updates and therefore require no physical gate execution. Consequently, the only physical operations applied to each qubit are the two \sqrt{X} gates shown in the circuit.

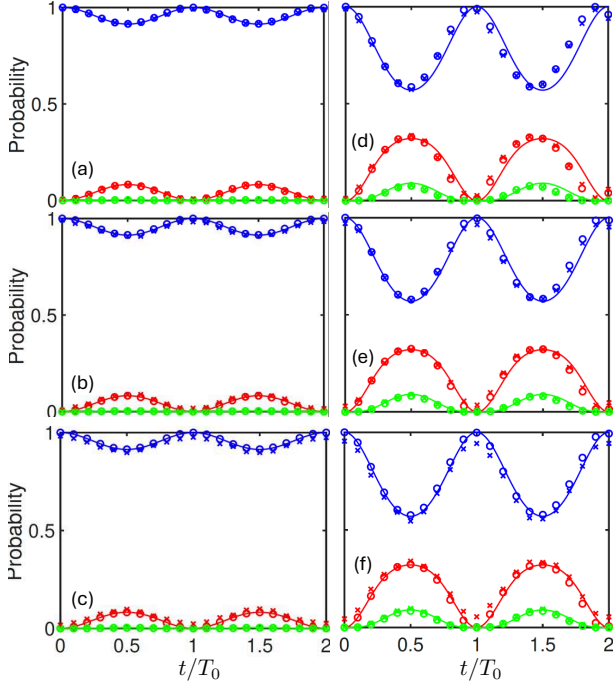


FIG. 3. Probabilities of the ground state (blue, top), first excited state (red, middle), and second excited state (green, bottom) of the driven harmonic oscillator as functions of t/T_0 . Solid lines: the analytical results for an ideal harmonic oscillator $P_b^{(n)}$; circles: the ideal qubit ensemble simulated with Qiskit Aer $P_c^{(n)}$; and crosses: results from noisy qubits on IBM Torino $P_q^{(n)}$. Panels (a-c) correspond to $F = 0.3$ with $N = 3, 5, 7$ qubits, while panels (d-f) correspond to $F = 0.75$ with $N = 6, 11, 16$ qubits, respectively. The detuning is $\Delta = 1$, and $T_0 = \pi/\Omega$ denotes the oscillation period.

In the simulations, we set the detuning $\Delta = 1$ and choose a driving amplitude $F < \Delta$ to ensure that the mean excitation number of the harmonic oscillator (or qubit ensemble) remains below 1. Figure 3 shows the time evolution of the probabilities for the ground state $|\frac{N}{2}, -\frac{N}{2}\rangle$ (corresponding to the oscillator ground state $|0\rangle$), the first excited state $|\frac{N}{2}, -\frac{N}{2} + 1\rangle$ ($|1\rangle$), and the second excited state $|\frac{N}{2}, -\frac{N}{2} + 2\rangle$ ($|2\rangle$). For each time t , the evolution is repeated 4096 times, and the probabilities are obtained by averaging the measurement outcomes. The differences between the probabilities from the ideal harmonic oscillator and those from the ideal qubit ensemble arise from the approximation in Eq. (3) for the HP mapping in the limit of $N \gg \langle a^\dagger a \rangle$. Accordingly, this discrepancy is more pronounced for smaller ensemble sizes and gradually diminishes as N increases. As shown in Figs. 3(c) and 3(f), these differences become negligible when either the driving strength is small ($F = 0.3$) or the ensemble size is large ($N = 18$). Meanwhile, the discrepancies between the results obtained from the ideal qubit ensemble and those from quantum hardware originate from imperfections of the real device, and accumulate as the system size N increases. Since

this simulation involves only single-qubit operations with small gate errors, the dominant hardware-induced error arises from qubit readout inaccuracy. On IBMQ, the typical error rate of the \sqrt{X} gates is around 3×10^{-4} , whereas the readout error rate is around 7.5×10^{-3} . The device calibration data for the qubits used in these experiments are summarized in Table I of Appendix A.

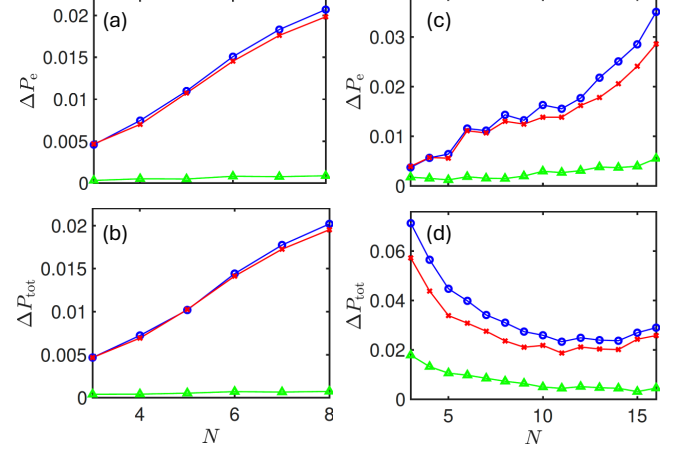


FIG. 4. (a, c) Probability difference $\Delta P_e^{(n)}$ as a function of qubit number N for $F = 0.3$ and $F = 0.75$, respectively. (b, d) Probability difference $\Delta P_{\text{tot}}^{(n)}$ as a function of N for $F = 0.3$ and $F = 0.75$, respectively. Top lines and circles (blue) correspond to the ground state; middle lines and crosses (red) correspond to the first excited state; and bottom lines and triangles (green) correspond to the second excited state. The lines are drawn to guide the eye, while the symbols (circles, crosses, and triangles) represent simulation results.

To quantify the interplay between algorithmic errors arising from the HP mapping and circuit errors originating from the quantum hardware, we first define the averaged probability difference that characterizes the effect of hardware-induced circuit errors:

$$\Delta P_e^{(n)} = \frac{1}{M} \sum_{j=1}^M \left| P_c^{(n)}(t_j) - P_q^{(n)}(t_j) \right|, \quad (11)$$

where $P_c^{(n)}$ denotes the probability of the state with n excitations obtained from the classical simulation of ideal qubits as defined in Eq. (10), $P_q^{(n)}$ is the corresponding probability obtained from the quantum simulation on noisy qubits in the quantum hardware, t_j is the j th time point, and M is the total number of sampled time points during the evolution. We further define the averaged probability difference that describes the combined effect of the algorithmic errors and the hardware-induced errors:

$$\Delta P_{\text{tot}}^{(n)} = \frac{1}{M} \sum_{j=1}^M \left| P_b^{(n)}(t_j) - P_q^{(n)}(t_j) \right|, \quad (12)$$

where $P_b^{(n)}$ is the exact probability for the harmonic oscillator defined in Eq. (7). The quantity $\Delta P_{\text{tot}}^{(n)}$ captures

the total deviation in simulating an oscillator mode on a quantum processor, incorporating both algorithmic and hardware-induced errors.

Figure 4 shows $\Delta P_e^{(n)}$ and $\Delta P_{\text{tot}}^{(n)}$ as functions of the number of qubits N for $F = 0.3$ and $F = 0.75$, respectively. As N increases, the circuit error $\Delta P_e^{(n)}$ grows monotonically, reflecting the accumulation of gate and measurement errors with increasing system size. In contrast, the algorithmic error decreases with increasing N and vanishes in the limit $N \gg n$. Consequently, the total deviation $\Delta P_{\text{tot}}^{(n)}$ between the harmonic oscillator and the quantum hardware results exhibits a minimum near $N \approx 12$ for $F = 0.75$ [Fig. 4(d)], arising from the competition between algorithmic and circuit errors. For the weaker driving strength $F = 0.3$, the algorithmic error remains negligible due to the small excitation number, and $\Delta P_{\text{tot}}^{(n)}$ is dominated entirely by circuit errors. These results demonstrate that increasing the system size does not necessarily improve simulation accuracy, highlighting the trade-off between algorithmic approximations and hardware noise in near-term quantum simulations. We note that the actual hardware execution time remains the same across the entire range of evolution time t , as the circuit depth is fixed for all values of t . Therefore, the accumulated circuit error does not increase with the simulated evolution time. Under these conditions, it is appropriate to quantify the simulation accuracy using the averaged probability differences, which provide a more reliable measure by incorporating information from multiple time points throughout the evolution.

IV. DIGITAL SIMULATION OF THE JC MODEL

A. Model

The minimal model describing the interaction between a single bosonic mode (cavity) and a quantum two-level system (qubit) is the JC model, governed by the Hamiltonian

$$H = \omega_0 a^\dagger a + \frac{\omega_z}{2} \tau_z + g (a \tau_+ + a^\dagger \tau_-), \quad (13)$$

where τ_z and τ_\pm are the Pauli operators of the qubit, ω_z is the qubit energy splitting, and g is the coupling strength between the qubit and the cavity mode. The JC model plays a central role in quantum optics and quantum information, exhibiting rich coherent dynamics that have been experimentally demonstrated in both atomic and solid-state quantum systems [62]. For the initial state $|0, \uparrow_\tau\rangle$, where the qubit is in the spin-up state and the cavity is in its vacuum state, the system undergoes vacuum Rabi oscillations between the states $|0, \uparrow_\tau\rangle$ and $|1, \downarrow_\tau\rangle$. This dynamics corresponds to the coherent exchange of a single excitation between the qubit and the cavity. The probability that the system remains in the

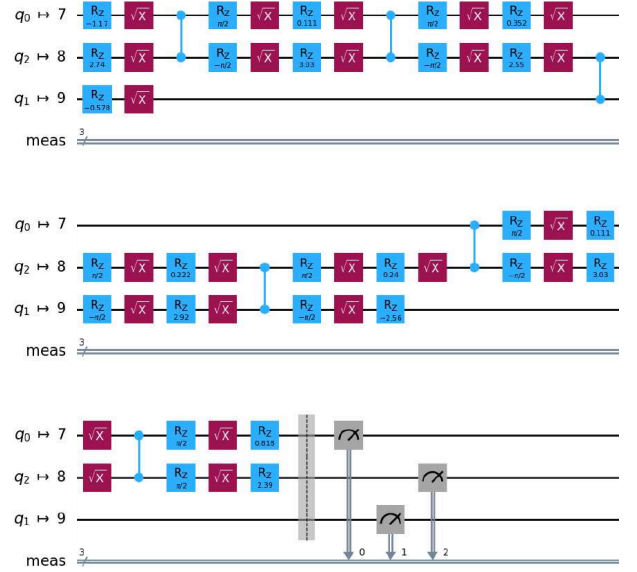


FIG. 5. Circuit diagram of a single Suzuki-Trotter step (up to a global phase of π) for the digital simulation of the JC model using two qubits to represent the cavity mode ($q_0 = \sigma_1$, $q_1 = \sigma_2$) and one qubit coupled to the cavity mode ($q_2 = \tau$). The circuit is transpiled into the native IBMQ gate set and followed by qubit measurements. The solid bars connecting pairs of qubits denote CZ gates. The phases of the R_z gates correspond to the parameters $\omega_0 = \omega_z = 1.0$, $g = 0.1$, and evolution time $t = \pi$.

state $|0, \uparrow_\tau\rangle$ at time t is

$$P_b^{(\uparrow)}(r) = \cos^2(\Omega_R t) + \sin^2(\Omega_R t) \left(\frac{\omega_z - \omega_0}{2\Omega_R} \right)^2 \quad (14)$$

with the Rabi frequency $\Omega_R = \sqrt{g^2 + (\omega_z - \omega_0)^2/4}$.

Using the HP transformation in Eq. (3), the cavity mode can be mapped onto a qubit ensemble. The JC Hamiltonian in Eq. (13) then takes the form

$$H = \frac{\omega_0}{2} \sum_{i=1}^N \sigma_{iz} + \frac{\omega_z}{2} \tau_z + \frac{g}{2\sqrt{N}} \sum_{i=1}^N (\sigma_{ix} \tau_x + \sigma_{iy} \tau_y), \quad (15)$$

where the constant term $\frac{N}{2}\omega_0$ has been omitted. In contrast to the driven harmonic oscillator case, the JC Hamiltonian contains interactions between the cavity qubits (described by the σ_i operators) and the qubit coupled to the cavity mode (described by the τ operators). These interactions can be expressed in the form of XX and YY couplings. Implementing this Hamiltonian therefore requires two-qubit quantum logic gates. Moreover, the interaction terms do not commute. For example, the interaction between cavity qubit σ_1 and τ does not commute with the interaction between cavity qubit σ_2 and τ . To realize the dynamics of this Hamiltonian on IBMQ, we develop two approaches: a Trotterization-based approach and a synthesized unitary method, as discussed below.

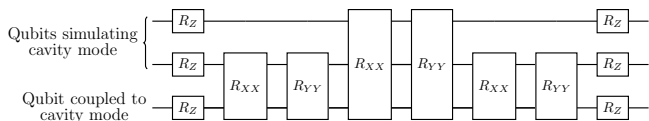
B. Trotterization and Implementation

The Trotter decomposition provides an effective method for approximating time evolution when the Hamiltonian consists of noncommuting terms that cannot be implemented simultaneously. By dividing the total evolution time t into K_T small intervals of duration t/K_T , the total time-evolution operator can be approximated as a product of exponentials of the individual Hamiltonian components [32]. The accuracy of this approximation systematically improves with higher-order decompositions. The standard (first-order) Trotter expansion, $e^{(A+B)t} \approx (e^{At/K_T} e^{Bt/K_T})^{K_T}$, introduces an error that scales as $(t/K_T)^2$. In contrast, the Suzuki-Trotter symmetrized (second-order) decomposition, $e^{(A+B)t} \approx (e^{At/2K_T} e^{Bt/K_T} e^{At/2K_T})^{K_T}$, reduces the error scaling to $(t/K_T)^3$, providing a significantly more accurate approximation of the time evolution [57].

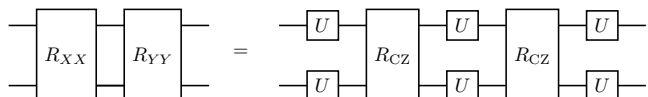
In this work, we adopt the Suzuki-Trotter decomposition to implement the JC Hamiltonian on IBMQ. For $\omega_0 = \omega_z = 1$ and $H_0 = \frac{\omega_0}{2} (\sum_{i=1}^N \sigma_{iz} + \tau_z)$, the JC Hamiltonian in the rotating frame defined by H_0 reduces to the interaction term given in Eq. (15). We use two qubits to represent the cavity mode, i.e., $N = 2$. The corresponding Suzuki-Trotter expansion of the rotating-frame Hamiltonian H_{rot} then takes the form:

$$e^{-itH_{\text{rot}}} \approx \left(e^{-iH_1 \frac{t}{2K_T}} e^{-iH_2 \frac{t}{K_T}} e^{-iH_1 \frac{t}{2K_T}} \right)^{K_T}, \quad (16)$$

where H_1 and H_2 denote the noncommuting components of H_{rot} : H_1 describes the coupling between cavity qubit σ_1 and the qubit τ , while H_2 accounts for the interaction between cavity qubit σ_2 and τ . Each Suzuki-Trotter step can be implemented using the following circuit:



which includes single-qubit R_Z gates and the two-qubit gates $R_{XX}(\theta) = e^{-i\frac{\theta}{2} X_1 \otimes X_2}$ and $R_{YY}(\theta) = e^{-i\frac{\theta}{2} Y_1 \otimes Y_2}$. When transpiled into the native IBMQ basis set, the combination of one R_{XX} and one R_{YY} operation can be implemented using two Controlled-Z (CZ) gates, together with several single-qubit rotations denoted by U :



The complete circuit diagram of a single Suzuki-Trotter step is shown in Fig. 5, where all single-qubit operations are decomposed into R_Z and \sqrt{X} gates.

To simulate the vacuum Rabi oscillation between the states $|0, \uparrow_\tau\rangle$ and $|1, \downarrow_\tau\rangle$ in the JC model, the qubit is initialized in the spin-up state, and the N qubits representing the cavity mode are initialized in the spin-down state.

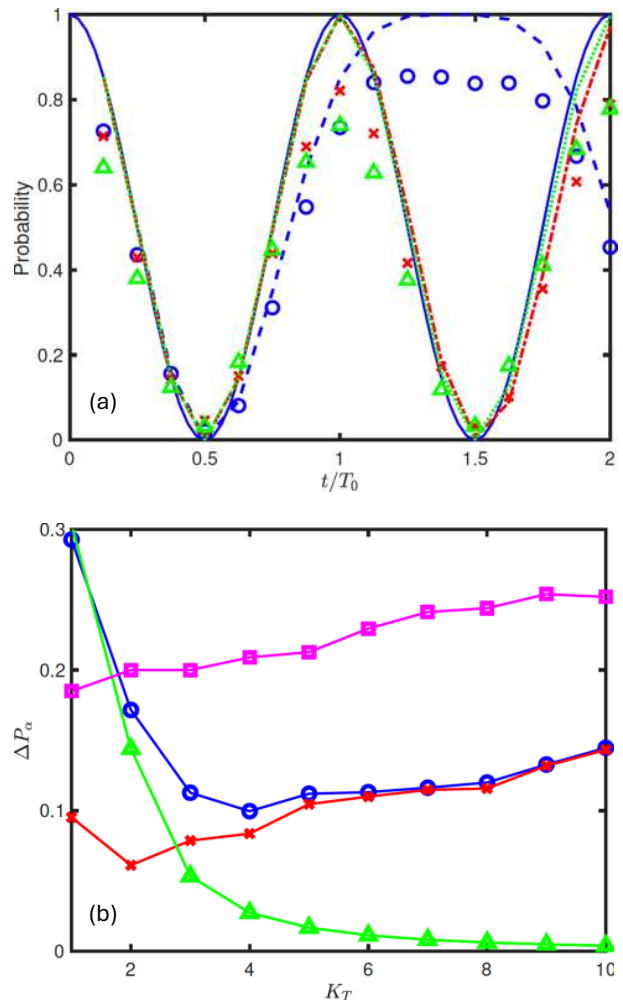


FIG. 6. (a) Probability of the state $|0, \uparrow_\tau\rangle$ vs time t/T_0 using Trotterization. Blue dashed line (circles): $K_T = 1$ from the ideal qubit ensemble (IBMQ); red dash-dotted line (crosses): $K_T = 4$ from the ideal qubit ensemble (IBMQ); and green dotted line (triangles): $K_T = 7$ from the ideal qubit ensemble (IBMQ). The blue solid line corresponds to the analytical result for an ideal cavity. And $T_0 = \pi/\Omega_R$ denotes the oscillation period. (b) Probability difference ΔP_α vs the number of Trotter steps K_T , with $\alpha = \text{tot}, e, a$. Blue circles: ΔP_{tot} ; red crosses: ΔP_e ; green triangles: ΔP_a ; and magenta squares: ΔP_e obtained from CZ-gate benchmarking in Sec. IV D. The solid lines are drawn to guide the eye. The simulation parameters are the same as in Fig. 5, with $\omega_0 = \omega_z = 1.0$ and $g = 0.1$.

We then apply the Trotterized circuit for a given evolution time t , spanning up to two full oscillation periods, followed by qubit measurements to obtain the probability of the state $|0, \uparrow_\tau\rangle$. For each value of t , the experiment is repeated 2,000 times to obtain the averaged probability. We measure this probability for $K_T = 1-7$ Trotter steps to investigate the interplay between algorithmic and hardware-induced errors, analogous to the analysis performed for the driven harmonic oscillator in Sec. III. For this circuit, the dominant hardware error arises from

the CZ gates with an error rate around 3×10^{-2} (see Table II of Appendix A).

Figure 6(a) shows the simulated probability of the state $|0, \uparrow_T\rangle$ as a function of t/T_0 , where T_0 denotes the oscillation period. It can be seen that as the number of Trotter steps increases, the algorithmic error associated with finite Trotter decomposition decreases, while the circuit error grows due to the increased circuit depth, in particular, due to the larger number of two-qubit CZ gates. To quantify this trade-off, we plot in Fig. 6(b) the probability differences as functions of the number of Trotter steps K_T . The total probability difference ΔP_{tot} , defined in Eq. (12), represents the average deviation between the results from the ideal cavity mode and those obtained from IBMQ simulations. The circuit error ΔP_e , defined in Eq. (11), quantifies the deviation between the ideal qubit ensemble and the hardware results, reflecting hardware-induced errors. The algorithmic error ΔP_a is defined as the difference between the ideal cavity and ideal qubit ensemble results with $\Delta P_a = \Delta P_{\text{tot}} - \Delta P_e$, and arises from the finite number of Trotter steps and the finite qubit ensemble size. Our results show that ΔP_e generally increases with K_T as the circuit depth (and thus accumulated gate error) grows, whereas ΔP_a decreases with K_T as the Trotter approximation improves. The total probability difference ΔP_{tot} exhibits an optimal minimum around $K_T \approx 4$, reflecting the interplay between algorithmic and hardware-induced errors, similar to the behavior observed for the driven harmonic oscillator in Sec. III.

C. Synthesized Unitary Approach and Implementation

In this section, we employ a synthesized unitary approach with a fixed quantum circuit layout, where a constant number of two-qubit gates are interleaved with single-qubit rotations containing tunable parameters [58–61]. The parameters of the single-qubit gates are optimized using classical simulations to best reproduce the desired target unitary, which in this case corresponds to the time-evolution operator of the JC Hamiltonian at a given evolution time t . Each single-qubit gate is represented by a general single-qubit unitary operator:

$$U(\alpha, \beta, \gamma) = \begin{pmatrix} \cos \frac{\beta}{2} & -e^{i\gamma} \sin \frac{\beta}{2} \\ e^{i\alpha} \sin \frac{\beta}{2} & e^{i(\alpha+\gamma)} \cos \frac{\beta}{2} \end{pmatrix}, \quad (17)$$

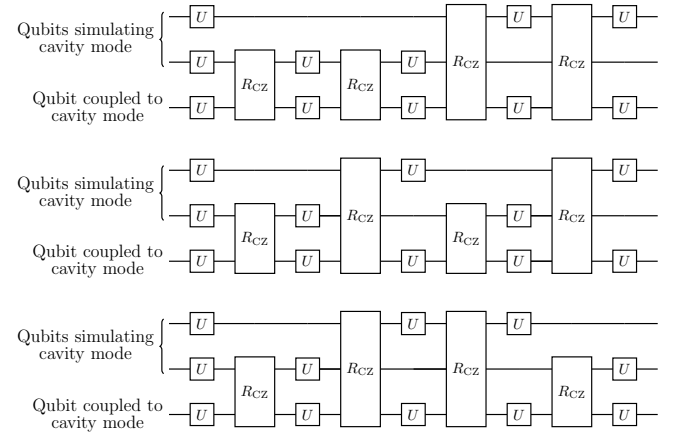
where the parameters α , β , and γ are numerically optimized following the standard U_3 -gate convention used in Qiskit. The cost function for the optimization is defined as $C = 1 - F$, where

$$F = \left| \frac{1}{2^{N+1}} \text{Tr} \left(U_f^\dagger U_T \right) \right|^2 \quad (18)$$

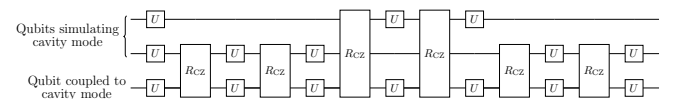
is the fidelity between the synthesized unitary transformation U_f and the target unitary transformation U_T at

a given time t with $N + 1$ being the total number of qubits in the simulated JC model. Using the limited-memory Broyden–Fletcher–Goldfarb–Shanno (L-BFGS) algorithm for optimization, we determine the optimal set of single-qubit rotation parameters that maximize F . In our implementation, the two-qubit gate is chosen to be the CZ gate to ensure compatibility with IBM Torino. Compared with the Suzuki-Trotter expansion method described in Sec. IV, the synthesized unitary approach requires only a fixed, small number of two-qubit gates and can be executed on a timescale comparable to that of a single Trotter step. In this way, the error arising from two-qubit operations is restricted, allowing significantly higher fidelity to be achieved. However, this method is limited to systems with a small number of qubits, since the classical computational cost of optimizing the circuit parameters increases exponentially with system size.

To implement the JC Hamiltonian with $N = 2$ qubits representing the cavity mode, we test circuit layouts containing either four or six CZ gates. The four-CZ-gate circuit employs the same number of two-qubit operations as a standard first-order (non-symmetrized) Trotter decomposition. We examine three distinct four-CZ-gate configurations, shown below:



These layouts are selected according to the following criteria: (1) each qubit representing the cavity mode participates in the same number of CZ gates; (2) every CZ gate couples one cavity-mode qubit with the qubit in the JC model; and (3) each layout is unique up to a reversal of the gate order or an exchange of the cavity-mode qubit indices, thereby eliminating redundant configurations. For each evolution time t , all three configurations are simulated, and the layout yielding the highest fidelity F is selected. The six-CZ-gate layout employs the same number of two-qubit operations as the Suzuki-Trotter decomposition and takes the following form:



This circuit layout is essentially identical to a single Suzuki-Trotter step for the JC model shown in Fig. 5,

except for the rotation phases of the single-qubit gates. Using this layout, we achieve very high gate fidelities, with $1 - F < 10^{-5}$ for arbitrary evolution times t .

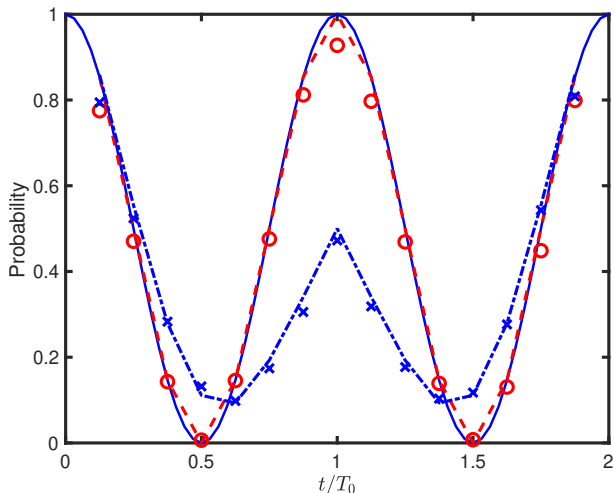


FIG. 7. Probability of the state $|0, \uparrow_\tau\rangle$ vs time t/T_0 using the synthesized unitary approach. Red dashed line (circles): six-CZ-gate layout from the ideal qubit ensemble (IBMQ); blue dash-dotted line (crosses): best four-CZ-gate layout from the ideal qubit ensemble (IBMQ). The blue solid line corresponds to the analytical result for an ideal cavity. All parameters are the same as in Fig. 6.

Using the optimized Δ parameters for the four-CZ-gate layouts and the six-CZ-gate layout, we simulate the vacuum Rabi oscillations studied in the previous subsections. Figure 7 shows the probability of the state $|0, \uparrow_\tau\rangle$ as a function of the evolution time t/T_0 for these different circuit layouts. As can be seen, the six-CZ-gate layout generally outperforms the four-CZ-gate layouts, producing higher accuracy with respect to the ideal cavity case. An exception occurs near the beginning and end of the evolution, where the four-CZ-gate layout achieves comparable accuracy and even outperforms the six-CZ-gate layout for quantum simulations on IBMQ owing to its shallower circuit depth. Compared with the Suzuki-Trotter decomposition, the six-CZ-gate layout yields significantly improved results. In the Trotter approach, the case with $K_T = 1$ Trotter step (six CZ gates) gives an average probability difference of $\Delta P_{\text{tot}} = 0.29$, and the optimal case with $K_T = 4$ (18 CZ gates) gives $\Delta P_{\text{tot}} = 0.10$. For the six-CZ-gate layout, the average probability difference is further reduced to $\Delta P_{\text{tot}} = 0.06$. The device calibration data for the qubits used in these experiments are summarized in Table III of Appendix A. These results show that for quantum simulation of small-sized systems, the synthesized unitary approach can outperform the Trotter approach, at the cost of additional classical computational resources for circuit optimization.

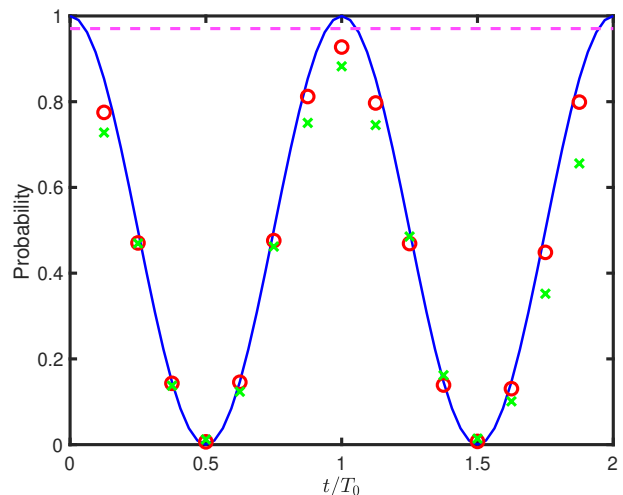


FIG. 8. Probability of the state $|0, \uparrow_\tau\rangle$ vs time t/T_0 for the six-CZ-gate layout of the synthesized unitary approach (red circles), the Suzuki-Trotter expansion with $K_T = 4$ (green crosses), and the benchmarking circuit containing only six CZ gates (magenta dashed horizontal line). The blue solid line corresponds to the analytical result for an ideal cavity. All parameters are the same as in Fig. 6.

D. Circuit Benchmarking with Only Two-Qubit Gates

On IBMQ, the dominant sources of circuit noise are two-qubit gates and measurements, with error rates ranging from 10^{-3} to 10^{-2} , whereas single-qubit gates exhibit error rates on the order of 10^{-4} . Moreover, two-qubit gates require approximately ten times longer execution times than single-qubit operations, increasing their susceptibility to decoherence arising from finite relaxation (T_1) and dephasing (T_2) times. To further assess the contribution of hardware noise, we perform an additional simulation using only two-qubit gates by removing all single-qubit rotations from the circuit in Fig. 5. On IBMQ, the native two-qubit gate is the CZ gate. For an ideal, noise-free circuit, each pair of CZ gates cancels, i.e., $R_{\text{CZ}}R_{\text{CZ}} = I$, where I denotes the identity operator. Therefore, any residual deviation observed in circuits containing an even number of CZ gates directly reflects the cumulative effects of hardware noise. The initial state of the simulation is $|0, \uparrow_\tau\rangle$, identical to that used in the JC model simulations in the previous subsections. We first apply six CZ gates, matching the number of two-qubit operations used in either a single Suzuki-Trotter step or the six-CZ-gate layout of the synthesized unitary approach. After executing this benchmarking circuit, we measure the probability of the state $|0, \uparrow_\tau\rangle$ over 2,000 repetitions and compute the averaged result. Figure 8 compares the measured probabilities obtained from the best Suzuki-Trotter result ($K_T = 4$), the synthesized unitary approach, and this benchmarking circuit. We find that the measured probability from this circuit is higher than those from both the Trotter and synthesized unitary

simulations at $t = T_0$ and $2T_0$. Meanwhile, the deviation of the probability in this circuit from the ideal value is comparable in magnitude to that obtained in the Trotter and synthesized unitary cases, confirming that this benchmarking circuit retains the dominant noise sources present in the quantum simulations discussed in the previous subsections. The device calibration data for the qubits used in this simulation are summarized in Table III of Appendix A.

We also perform simulations consisting of K_T repetitions of the six-CZ-gate sequence (i.e., a total of $6K_T$ CZ gates) using Qiskit for both ideal and noisy qubits, with the device calibration data listed in Table II. The probability difference ΔP_e between the noisy qubit simulation for this benchmarking circuit and the exact result is shown in Fig. 6(b) (magenta squares). As seen from the figure, ΔP_e increases approximately linearly with K_T , exhibiting the same trend as observed in the Trotter simulation (red crosses). The magnitude of ΔP_e for this benchmarking circuit is larger than that in the Trotter case. This difference arises because, in the benchmarking circuit, the probability deviation is evaluated at $t = T_0$ and $2T_0$, where the discrepancy from the exact result is maximal, as observed in Fig. 8(a). In contrast, the Trotter results are averaged over the full time evolution, which reduces the overall magnitude of the probability difference.

V. CONCLUSIONS

In this work, we have demonstrated the digital quantum simulation of the HP transformation on a cloud-based superconducting quantum processor, where a bosonic mode is mapped onto and emulated by a spin ensemble. Two representative models were investigated: the driven harmonic oscillator and the JC model, which together capture the essential features of bosonic dynamics and light-matter interaction. For the driven harmonic oscillator, our results reveal the interplay between algorithmic errors arising from the finite size of the qubit ensemble and circuit errors dominated by measurement noise, leading to an optimal ensemble size for achieving high-fidelity simulations. For the JC model, we employed two distinct approaches, the Suzuki-Trotter decomposition and the synthesized unitary approach, and observed a trade-off between algorithmic errors and hardware-induced noise. By further benchmarking circuits containing only two-qubit gates, we identified two-qubit gate errors as the dominant source of circuit noise. Overall, our study establishes a practical framework for implementing HP mappings and simulating bosonic modes on digital quantum processors. These methods can be extended to emulate more complex spin-boson and multi-mode cavity models, paving the way for quantum simulation of many-body systems involving bosonic degrees of freedom in the NISQ era. In addition, our findings provide valuable insights into algorithm-hardware co-design

strategies aimed at optimizing the fidelity, efficiency, and scalability of digital quantum simulations involving collective spin and bosonic modes.

ACKNOWLEDGMENTS

K.Y., A.M., and L.T. acknowledge support from the National Science Foundation under Awards DMR-2037987 and CICI-2530705. S.A. was supported by Japan’s Ministry of Education, Culture, Sports, Science and Technology (MEXT) Quantum Leap Flagship Program under Grant No. JPMXS0120319794. K.Y. and L.T. thank NICT for hospitality.

Appendix A: Circuit Data of IBMQ Backend

In this Appendix, we present device calibration data for qubits in the quantum backend (IBM Torino) used in the quantum simulations of this work.

qubit index	readout error	SX error	$T_1(\mu s)$	$T_2(\mu s)$
81	0.00439	0.00035	193	139
54	0.00549	0.00032	118	58
87	0.00562	0.00017	118	126
36	0.00623	0.00047	87	97
28	0.0072	0.00023	127	115
110	0.00745	0.0003	216	114
11	0.00757	0.00018	117	150
17	0.00757	0.00045	146	69
18	0.00781	0.00033	217	125
117	0.00806	0.0004	114	89
125	0.00842	0.00055	184	132
66	0.00891	0.00027	200	143
45	0.00903	0.00049	42	46
51	0.00903	0.00031	155	109

TABLE I. Calibration data for the qubits used in Sec. III. The device characterization was performed on October 28, 2025.

For the driven quantum harmonic oscillator circuit, we utilized up to 18 qubits on IBM Torino. The qubit indices, readout error rates, single-qubit gate error rates, and coherence times (T_1 and T_2) are summarized in Table I.

For the JC model, we employed two qubits to represent the cavity mode and one additional qubit to couple to the cavity and form the JC system. The calibration data for these qubits in the Suzuki-Trotter decomposition are provided in Table II. The calibration data for these qubits in the synthesized unitary approach are provided in Table III.

For the CZ-gate-only testing circuit discussed in Sec. IV D, a total of three qubits were employed to match the circuit depth and qubit count used in the JC model simulation. The calibration data for the qubits used for Fig. 8 are summarized in Table III. The calibration data for the qubits used for the magenta squares in Fig. 6(b) are summarized in Table II.

qubit index	readout error	R_{CZ} error	SX error	$T_1(\mu s)$	$T_2(\mu s)$
O: 7	0.0017	0.038	0.0006	147	122
O: 9	0.0019	0.026	0.0002	189	164
A: 8	0.0036		0.0004	194	218

TABLE II. Calibration data for the qubits used in Sec. IV B. “O” refers to the qubits used to simulate the cavity mode, and “A” refers to the qubit coupled to the cavity mode. The device characterization was performed on September 2, 2025.

qubit index	readout error	R_{CZ} error	SX error	$T_1(\mu s)$	$T_2(\mu s)$
O: 55	0.0109	0.0044	0.00048	181	72
O: 66	0.0057	0.0015	0.00021	143	85
A: 65	0.015		0.00018	182	199

TABLE III. Calibration data for the qubits used in Sec. IV C and Sec. IV D. The device characterization was performed on November 4, 2025.

In addition, the simulation of the JC model involves both single-qubit and two-qubit quantum logic gates. For single-qubit operations, only the SX (\sqrt{X}) gate is physically executed, whereas the R_Z gate is implemented vir-

tually as a frame change. Two-qubit gates have substantially longer execution times and are therefore more susceptible to circuit noise. On IBM Torino, all two-qubit operations are realized using the CZ gate in combination with single-qubit rotations. Table IV summarizes the total number of gates and the runtimes for the Suzuki-Trotter decomposition and the synthesized unitary approach, respectively.

Trotter or synthesized unitary	CZ gate count	SX gate count	runtime (μs)
1 Trotter step	6	22	3.9
2 Trotter steps	10	36	6.4
3 Trotter steps	14	50	9.0
4 Trotter steps	18	64	12
5 Trotter steps	22	78	14
6 Trotter steps	26	92	17
7 Trotter steps	30	106	19
synthesized four-CZ	4	20	2.7
synthesized six-CZ	6	28	4.1

TABLE IV. Gate counts and execution runtimes for the simulations in Sec. IV.

-
- [1] I. M. Georgescu, S. Ashhab, and F. Nori, Quantum simulation, *Reviews of Modern Physics* **86**, 153 (2014).
- [2] F. Tacchino, A. Chiesa, S. Carretta, and D. Gerace, Quantum computers as universal quantum simulators: state-of-the-art and perspectives, *Advanced Quantum Technologies* **3**, 1900052 (2020).
- [3] A. J. Daley, I. Bloch, C. Kokail, S. Flannigan, N. Pearson, M. Troyer, and P. Zoller, Practical quantum advantage in quantum simulation, *Nature* **607**, 667 (2022).
- [4] B. Fauseweh, Quantum many-body simulations on digital quantum computers: State-of-the-art and future challenges, *Nature Communications* **15**, 2123 (2024).
- [5] IBM Quantum Platform, see webpage at <https://quantum.cloud.ibm.com/>.
- [6] A. Kandala, A. Mezzacapo, K. Temme, M. Takita, M. Brink, J. M. Chow, and J. M. Gambetta, Hardware-efficient variational quantum eigensolver for small molecules and quantum magnets, *Nature* **549**, 242 (2017).
- [7] P. Frey and S. Rachel, Realization of a discrete time crystal on 57 qubits of a quantum computer, *Science Advances* **8**, eabm7652 (2022).
- [8] Y. Kim, A. Eddins, S. Anand, K. X. Wei, E. van den Berg, S. Rosenblatt, H. Nayfeh, Y. Wu, M. Zaletel, K. Temme, and A. Kandala, Evidence for the utility of quantum computing before fault tolerance, *Nature* **618**, 500 (2023).
- [9] N. Yoshioka, M. Amico, W. Kirby, P. Jurcevic, A. Dutt, B. Fuller, S. Garion, H. Haas, I. Hamamura, A. Ivrii, R. Majumdar, Z. Mineev, M. Motta, B. Pokharel, P. Rivero, K. Sharma, C. J. Wood, A. Javadi-Abhari, and A. Mezzacapo, Krylov diagonalization of large many-body hamiltonians on a quantum processor, *Nature Communications* **16**, 5014 (2025).
- [10] L. B. Oftelie, M. Urbanek, M. Metcalf, J. Carter, A. F. Kemper, and W. A. de Jong, Simulating quantum materials with digital quantum computers, *Quantum Sci. Technol.* **6**, 043002 (2021).
- [11] J. Abhijith, A. Adedoyin, J. Ambrosiano, P. Anisimov, W. Casper, G. Chennupati, C. Coffrin, H. Djidjev, D. Gunter, S. Karra, N. Lemons, S. Lin, A. Malyzhenkov, D. Mascarenas, S. Mniszewski, B. Nadiga, D. O’malley, D. Oyen, S. Pakin, L. Prasad, R. Roberts, P. Romero, N. Santhi, N. Sinitsyn, P. J. Swart, J. G. Wendelberger, B. Yoon, R. Zamora, W. Zhu, S. Eidenbenz, A. Bäertschi, P. J. Coles, M. Vuffray, and A. Y. Lohkov, Quantum algorithm & implementations for beginners, *ACM Trans. Quantum Comput.* **3**, 18 (2022).
- [12] L. Abdurakhimov *et al.*, Technology and performance benchmarks of IQM’s 20-qubit quantum computer (2024), arXiv:2408.12433.
- [13] Qiskit Open-Source Quantum Software, see webpage at <https://qiskit.org/>.
- [14] H. Lamm and S. Lawrence, Simulation of nonequilibrium dynamics on a quantum computer, *Physical Review Letters* **121**, 170501 (2018).
- [15] A. Zhukov, S. Remizov, W. Pogosov, and Y. E. Lozovik, Algorithmic simulation of far-from-equilibrium dynamics using quantum computer, *Quantum Information Processing* **17**, 223 (2018).
- [16] A. Chiesa, F. Tacchino, M. Grossi, P. Santini, I. Tavernelli, D. Gerace, and S. Carretta, Quantum hardware simulating four-dimensional inelastic neutron scattering, *Nature Physics* **15**, 455 (2019).
- [17] A. Smith, M. Kim, F. Pollmann, and J. Knolle, Simulating quantum many-body dynamics on a current digital quantum computer, *npj Quantum Information* **5**, 106 (2019).
- [18] B. Fauseweh and J.-X. Zhu, Digital quantum simulation of non-equilibrium quantum many-body systems, *Quan-*

- tum Information Processing **20**, 138 (2021).
- [19] T. A. Chowdhury, K. Yu, M. A. Shamim, M. L. Kabir, and R. S. Sufian, Enhancing quantum utility: Simulating large-scale quantum spin chains on superconducting quantum computers, *Phys. Rev. Res.* **6**, 033107 (2024).
- [20] K. Georgopoulos, C. Emary, and P. Zuliani, Modeling and simulating the noisy behavior of near-term quantum computers, *Phys. Rev. A* **104**, 062432 (2021).
- [21] G. Di Bartolomeo, M. Vischi, F. Cesa, R. Wixinger, M. Grossi, S. Donadi, and A. Bassi, Noisy gates for simulating quantum computers, *Physical Review Research* **5**, 043210 (2023).
- [22] M. L. Dahlhauser and T. S. Humble, Modeling noisy quantum circuits using experimental characterization, *Physical Review A* **103**, 042603 (2021).
- [23] J. A. Bravo-Montes, M. Bastante, G. Botella, A. del Barrio, and F. García-Herrero, A methodology to select and adjust quantum noise models through emulators: benchmarking against real backends, *EPJ Quantum Technology* **11**, 71 (2024).
- [24] S. Bordoni, A. Papaluca, P. Buttarini, A. Sopena, S. Giagu, and S. Carrazza, Quantum noise modeling through reinforcement learning, *Quantum Science and Technology* **11**, 015005 (2025).
- [25] E. Magesan, J. M. Gambetta, and J. Emerson, Scalable and robust randomized benchmarking of quantum processes, *Phys. Rev. Lett.* **106**, 180504 (2011).
- [26] E. Desdentado, C. Calero, M. Á. Moraga, and F. García, Quantum computing software solutions, technologies, evaluation and limitations: a systematic mapping study, *Computing* **107**, 110 (2025).
- [27] H. T. Nguyen, P. Krishnan, D. Krishnaswamy, M. Usman, and R. Buyya, Quantum cloud computing: a review, open problems, and future directions (2024), arXiv:2404.11420.
- [28] K. Temme, S. Bravyi, and J. M. Gambetta, Error mitigation for short-depth quantum circuits, *Phys. Rev. Lett.* **119**, 180509 (2017).
- [29] A. He, B. Nachman, W. A. de Jong, and C. W. Bauer, Zero-noise extrapolation for quantum-gate error mitigation with identity insertions, *Phys. Rev. A* **102**, 012426 (2020).
- [30] E. Rosenberg, P. Ginsparg, and P. L. McMahon, Experimental error mitigation using linear rescaling for variational quantum eigensolving with up to 20 qubits, *Quantum Science and Technology* **7**, 015024 (2022).
- [31] Z. Cai, R. Babbush, S. C. Benjamin, S. Endo, W. J. Huggins, Y. Li, J. R. McClean, and T. E. O'Brien, Quantum error mitigation, *Rev. Mod. Phys.* **95**, 045005 (2023).
- [32] M. A. Nielsen and I. L. Chuang, *Quantum Computation and Quantum Information: 10th Anniversary Edition* (Cambridge University Press, 2010).
- [33] T. J. Stavenger, E. Crane, K. Smith, C. T. Kang, S. M. Girvin, and N. Wiebe, Bosonic Qiskit (2022), arXiv:2209.11153.
- [34] A. Mezzacapo, U. L. Heras, J. S. Pedernales, L. DiCarlo, E. Solano, and L. Lamata, Digital quantum Rabi and Dicke models in superconducting circuits, *Scientific Reports* **4**, 7482 (2014).
- [35] D. V. Babukhin, A. A. Zhukov, and W. V. Pogosov, Hybrid digital-analog simulation of many-body dynamics with superconducting qubits, *Physical Review A* **101**, 052337 (2020).
- [36] N. K. Langford, R. Sagastizabal, M. Kounalakis, C. Dickel, A. Bruno, F. Luthi, D. J. Thoen, A. Endo, and L. DiCarlo, Experimentally simulating the dynamics of quantum light and matter at deep-strong coupling, *Nature Communications* **8**, 1715 (2017).
- [37] D. S. Shapiro, Y. Weber, T. Bode, F. K. Wilhelm, and D. Bagrets, Digital-analog simulations of Schrödinger cat states in the Dicke-Ising model, *Phys. Rev. A* **112**, 042412 (2025).
- [38] A. Burger, L. C. Kwek, and D. Poletti, Digital quantum simulation of the spin-boson model under markovian open-system dynamics, *Entropy* **24**, 1766 (2022).
- [39] F. Mei, V. M. Stojanović, I. Siddiqi, and L. Tian, Analog superconducting quantum simulator for Holstein polarons, *Phys. Rev. B* **88**, 224502 (2013).
- [40] K. Seo and L. Tian, Quantum phase transition in a multiconnected superconducting Jaynes-Cummings lattice, *Phys. Rev. B* **91**, 195439 (2015).
- [41] K. Cai, P. Parajuli, G. Long, C. W. Wong, and L. Tian, Robust preparation of many-body ground states in Jaynes-Cummings lattices, *npj Quantum Information* **7**, 96 (2021).
- [42] K. Cai, P. Parajuli, A. Govindarajan, and L. Tian, Quantum shortcut to adiabaticity for state preparation in a finite-sized Jaynes-Cummings lattice, *Phys. Rev. A* **110**, 022621 (2024).
- [43] S. Somaroo, C. H. Tseng, T. F. Havel, R. Laflamme, and D. G. Cory, Quantum simulations on a quantum computer, *Phys. Rev. Lett.* **82**, 5381 (1999).
- [44] N. P. D. Sawaya, T. Menke, T. H. Kyaw, S. Johri, A. Aspuru-Guzik, and G. G. Guerreschi, Resource-efficient digital quantum simulation of d-level systems for photonic, vibrational, and spin-s hamiltonians, *npj Quantum Information* **6**, 49 (2020).
- [45] C. Sabín, Digital quantum simulation of linear and non-linear optical elements, *Quantum Reports* **2**, 208 (2020).
- [46] P. C. Encinar, A. Agustí, and C. Sabín, Digital quantum simulation of beam splitters and squeezing with ibm quantum computers, *Phys. Rev. A* **104**, 052609 (2021).
- [47] R. D. Somma, Quantum computation, complexity, and many-body physics (2005), arXiv:quant-ph/0512209.
- [48] A. Baishya, L. Kumar, B. K. Behera, and P. K. Panigrahi, Experimental demonstration of force driven quantum harmonic oscillator in ibm quantum computer (2019), arXiv:1906.01436.
- [49] S. Chin, J. Kim, and J. Huh, Quantum circuit simulation of linear optics using fermion to qubit encoding (2022), arXiv:2209.00207.
- [50] X.-Y. Huang, L. Yu, X. Lu, Y. Yang, D.-S. Li, C.-W. Wu, W. Wu, and P.-X. Chen, Qubitization of bosons (2022), arXiv:2105.12563.
- [51] M. K. Marinkovic and M. Radulaski, Singly-excited resonant open quantum system tavis-cummings model with quantum circuit mapping, *Scientific Reports* **13**, 19435 (2023).
- [52] A. H. Rubin, B. Marinelli, V. A. Norman, Z. Rizvi, A. D. Burch, R. K. Naik, J. Mark Kreikebaum, M. N. H. Chow, D. S. Lobser, M. C. Revella, C. G. Yale, M. Ivory, D. I. Santiago, C. Spitzer, M. Marinkovic, S. M. Clark, I. Siddiqi, and M. Radulaski, Digital quantum simulation of cavity quantum electrodynamics: insights from superconducting and trapped ion quantum testbeds, *Quantum Science and Technology* **10**, 045057 (2025).
- [53] T. Holstein and H. Primakoff, Field dependence of

- the intrinsic domain magnetization of a ferromagnet, *Phys. Rev.* **58**, 1098 (1940).
- [54] F. T. Arecchi, E. Courtens, R. Gilmore, and H. Thomas, Atomic coherent states in quantum optics, *Phys. Rev. A* **6**, 2211 (1972).
- [55] M. Tudorovskaya and D. Muñoz Ramo, Quantum computing simulation of a mixed spin-boson hamiltonian and its performance for a cavity quantum electrodynamics problem, *Phys. Rev. A* **109**, 032612 (2024).
- [56] N. Fitzpatrick, H. Apel, and D. M. Ramo, Evaluating low-depth quantum algorithms for time evolution on fermion-boson systems (2021), arXiv:2106.03985.
- [57] M. Suzuki, Fractal decomposition of exponential operators with application to many-body theories and Monte Carlo simulations, *Phys. Lett. A* **146**, 319 (1990).
- [58] T. Goubault de Brugière, M. Baboulin, B. Valiron, and C. Allouche, Synthesizing quantum circuits via numerical optimization, in *Computational Science–ICCS 2019: 19th International Conference, Faro, Portugal, June 12–14, 2019, Proceedings, Part II 19* (Springer, 2019) pp. 3–16.
- [59] S. Ashhab, N. Yamamoto, F. Yoshihara, and K. Semba, Numerical analysis of quantum circuits for state preparation and unitary operator synthesis, *Physical Review A* **106**, 022426 (2022).
- [60] S. Ashhab, F. Yoshihara, M. Tsuji, M. Sato, and K. Semba, Quantum circuit synthesis via a random combinatorial search, *Physical Review A* **109**, 052605 (2024).
- [61] P. Baßler, M. Zipper, C. Cedzich, M. Heinrich, P. H. Huber, M. Johanning, and M. Kliesch, Synthesis of and compilation with time-optimal multi-qubit gates, *Quantum* **7**, 984 (2023).
- [62] A. Blais, R.-S. Huang, A. Wallraff, S. M. Girvin, and R. J. Schoelkopf, Cavity quantum electrodynamics for superconducting electrical circuits: An architecture for quantum computation, *Phys. Rev. A* **69**, 62320 (2004).